Electron and proton aurora observed spectroscopically in the far ultraviolet

M. Galand,[1] D. Lummerzheim,[2] A. W. Stephan,[3,4] B. C. Bush,[5] and S. Chakrabarti[1]

[1] The only way to get a global, instantaneous picture of the energetic particle input over the auroral oval is through spectral imaging. The major driver of auroral emissions in the high-latitude ionosphere is overall electron precipitation. However, for certain locations and times, such as the equatorial edge of the evening auroral oval, proton precipitation can be the major energy source and thus the primary contributor to auroral emissions. Using kinetic transport models to describe the transport of energetic particles in the atmosphere, we analyze UV spectra from the STP78-1 satellite mission during magnetically disturbed conditions ($Kp = 6$) in the evening sector of the auroral oval. We discuss the contribution of protons and electrons to the auroral emissions. The energy flux of the incident protons is inferred from the H Lyman α emissions, after removing the H geocoronal background induced by solar radiation. Both the mean energy and energy flux of electron precipitation are inferred from non-H emissions (N II 108.5 nm, N_2 135.4 nm, and O I 135.6 nm), after removing the contribution of proton precipitation. From the latitudinal distribution of the incident energy flux the location of the electron and proton aurorae is discussed. The estimation of the particle characteristics allows one to infer the Pedersen and Hall electrical conductances induced by particle precipitation. For the studied substorm period, energetic protons contribute significantly to the Pedersen conductance, $\sim 25-30\%$ overall of the total particle-induced conductances and much more at the equatorward edge of the midnight aurora. Because protons and electrons do not interact in the same way with the atmosphere, our study shows that while analyzing auroral spectra and studying the state of the ionosphere, it is crucial to separate electron and proton components of the precipitation. The method described to disentangle the relative contribution of precipitating electrons and protons may be applicable to the UV data of the upcoming TIMED and DMSP missions. *INDEX TERMS:* 2407 Ionosphere: Auroral ionosphere (2704); 2455 Ionosphere: Particle precipitation; 2431 Ionosphere: Ionosphere/magnetosphere interactions (2736); *KEYWORDS:* proton aurora, FUV aurora, inversion, conductance

1. Introduction

[2] Energetic electrons and protons precipitating from the magnetosphere are a major energy source in the high-latitude regions inducing significant ionospheric and thermospheric perturbations [e.g., *Rees*, 1989]. Aurora is the optical manifestation of the interaction of these energetic particles with atmospheric neutrals. Spectral characteristics of auroral emissions can be used to remotely sense the particle characteristics for estimation of the subsequent atmospheric response or for tracking magnetospheric processes.

[3] Imaging auroral emissions from space is the only way to get a global snapshot of the particle energy over the high-latitude regions. Polar/UltraViolet Imager (UVI) and Polar/Visible Imaging System (VIS) images were used to retrieve the electron characteristics over the auroral ovals from N_2 Lyman-Birge-Hopfield (LBH) brightnesses [e.g., *Germany et al.*, 1997; *Lummerzheim et al.*, 1997] and from the visible O I 630.0 nm and N_2^+ first negative brightnesses [e.g., *Frank et al.*, 1995], respectively. The mean energy of the incident electrons is retrieved from the brightness ratio in two different wavelength regions while the incident energy flux from the total brightness in a given spectral window. Such information over the entire auroral oval is crucial for estimating the overall energy budget during a magnetic cloud event [*Lu et al.*, 1998] or for studying the magnetospheric source regions of auroral precipitation and field-aligned currents during a substorm [*Lu et al.*, 2000]. Overall, most of the energy is carried by electrons. However, for certain regions of the auroral oval, such as the equatorward part of the evening sector, protons are a major energy source [*Hardy et al.*, 1989], that is, a significant ionization [*Galand et al.*, 2001] and excitation [*Lummerzheim et al.*, 2001]

[1]Center for Space Physics, Boston University, Boston, Massachusetts, USA.
[2]Geophysical Institute, University of Alaska, Fairbanks, Alaska, USA.
[3]Computational Physics, Inc., Springfield, Virginia, USA.
[4]Formerly at Center for Space Physics, Boston University, Boston, Massachusetts, USA.
[5]Atmospheric Research Laboratory, Scripps Institute of Oceanography, University of California, San Diego, California, USA.

source. Because they do not deposit their energy in the same way as electrons [*Galand et al.*, 1999], it is necessary to treat the proton component separately.

[4] H emissions are a unique signature of proton precipitation. They result from excited H atoms inside the proton beam. In the region where precipitating particles deposit their energy (100–300 km altitude), the ambient H atom density is too low to produce a significant amount of auroral emissions from excitation by energetic particle precipitation. Since the hydrogen atoms retain the energy of the protons on charge exchange, the emissions of excited H atoms are Doppler broadened and shifted. The ground-based discovery of these emissions was the first evidence of the presence of proton precipitation in high latitudes [*Vegard*, 1948]. Further observations of proton aurora Balmer lines (H_α, H_β) were undertaken from ground [e.g., *Meinel*, 1951; *Eather*, 1967; *Wiens and Vallance-Jones*, 1969; *Vallance-Jones et al.*, 1982; *Lorentzen et al.*, 1998; *Deehr and Lummerzheim*, 2001; *Lummerzheim and Galand*, 2001; *Takahashi and Fukunishi*, 2001, and references therein]. Several rocket campaigns were dedicated to proton aurora study [e.g., *Romick and Sharp*, 1967; *Whalen et al.*, 1967; *Miller and Shepherd*, 1969; *Reasoner et al.*, 1968; *Søraas et al.*, 1974]. The combination of in situ measurements of energetic particles with rocket-based or coincident ground-based photometric observations of H Balmer emissions during these rocket campaigns provided some constraints on the proton aurora modeling.

[5] Satellite missions have also been major contributors to the study of proton aurora through Far UltraViolet (FUV) measurements of H Ly α, the strongest H emissions in proton aurora [e.g., *Ishimoto et al.*, 1989; *Paresce et al.*, 1983; *Bertaux et al.*, 1984; *Strickland et al.*, 2001, and references therein]. Such an approach provides a unique opportunity to observe large portions of the auroral oval, as illustrated by the Polar Beacon Experiment and Auroral Research (Polar BEAR) images of H Ly α [*Strickland et al.*, 2001]. Recently, Imager for Magnetopause to Aurora Global Exploration (IMAGE) offered the first snapshots of the entire proton auroral oval [*Mende et al.*, 2001]. Spectral filtering is applied with a passband centered at a Doppler-shifted Ly α wavelength to remove any emission from the geocorona. A preliminary analysis of the Ly α data along with auroral non-H emissions (induced by both electron and proton precipitations) is presented by *Frey et al.* [2001]. They compared FUV observations with modeled brightnesses derived from Fast Auroral Snapshot (FAST) particle data and found a good quantitative agreement between both data sets.

[6] The first comprehensive analysis of FUV spectra of combined electron/proton aurora was performed by *Strickland et al.* [2001] using Midcourse Space Experiment (MSX)/ Ultraviolet and Visible Imaging and Spectrographic Imaging (UVISI) limb observations for quiet magnetic conditions. For the analysis the authors used the electron and proton transport codes from *Basu et al.* [1993]. Assuming a mean energy for both the incident electrons and protons, they retrieved the particle energy fluxes from limb profiles for one given scan through the aurora. They assumed a uniform precipitation, which results in some limitations to the analysis as viewing is across the aurora and as the spatial distribution of the precipitation is not uniform.

[7] In this paper we provide a comprehensive analysis of near-nadir FUV spectra acquired by the STP78-1 satellite for one poleward pass over the southern auroral oval during active magnetic conditions. Unlike the Advanced Research Global Observation Satellite (ARGOS)/ High Resolution Airglow and Aurora Spectroscopy (HIRAAS) instrument which obtains spectra no closer than $63°$ to nadir, the STP78-1 satellite has provided FUV spectra, including H Ly α, covering all viewing angles that reaches $30°$ to zenith and nadir. Thus it offers a more suitable data set for inferring the characteristics of both precipitating electrons and protons from FUV emissions. H Ly α emission is used to retrieve the incident proton energy flux. Both the mean energy and energy flux of electron precipitation are inferred from non-H emissions (N II 108.5 nm, N_2 135.4 nm, and O I 135.6 nm), after removing the contribution from proton precipitation. We first present the data set and explain how the geocoronal background is removed from the H Ly α spectra. We next discuss auroral emission yields computed with combined electron [*Lummerzheim et al.*, 1989] and proton [*Galand et al.*, 1997] transport codes. Finally, we assess the characteristics of the incident energetic electrons and protons, by applying the modeling results to observed spectra. We propose a validation of the approach by comparing the simulated and measured spectra in the vicinity of H Ly β and O I 102.7 nm emissions. We discuss the latitudinal extent of electron and proton aurora and estimate the Pedersen and Hall conductances induced by particle precipitation.

2. Data Description

2.1. Overview of the Data

[8] The FUV spectrograph orbited the Earth aboard the U.S. Air Force STP78-1 satellite. The 600-km altitude circular orbit had an inclination of $97.9°$ and an orbital period of 96 min. This orbit was Sun-synchronous along the noon-midnight meridian, with a precession of $1°$ per day. The satellite tumbled in its orbit with the spin axis parallel to the axis of the orbital plane. The spectrograph was housed in the spinning wheel of the spacecraft, pointed out $30°$ from the orbital plane and sweeping out a cone as the satellite tumbled in its orbit. The instrument's line of sight was oriented $120°$ from the spin axis. Figure 1 illustrates this viewing geometry. The viewing angles ranged from $\sim30°$ to $150°$ relative to the local zenith and were never closer than $30°$ to the Sun. The intrinsic field of view of $7° \times 9°$ in combination with the telemetry rate and the cartwheeling motion of the spacecraft (at a spin rate of 11 revolutions per minute) provided a working field of view of $18° \times 9°$. The bandpass covered the FUV range from 80 to 140 nm with a full width half maximum (FWHM) of 0.8 ± 0.1 nm according to laboratory measurements. The value of 0.8 nm was confirmed by the analysis of the geocoronal H Ly α observed when the instrument was pointed downward in the midlatitude nightside region. The spectrograph was calibrated in the laboratory before flight and was found to have a sensitivity of 0.07 count $s^{-1} R^{-1}$ at 80 nm, dropping slowly to ~0.01 count $s^{-1} R^{-1}$ at 140 nm [*Chakrabarti et al.*, 1983]. The uncertainty in calibration was 20% at wavelengths shorter than 120 nm and reached 50% at 140 nm. Each electronic wavelength bin was ~0.5 nm wide. A complete description of the instrument is given by *Bowyer et al.* [1981].
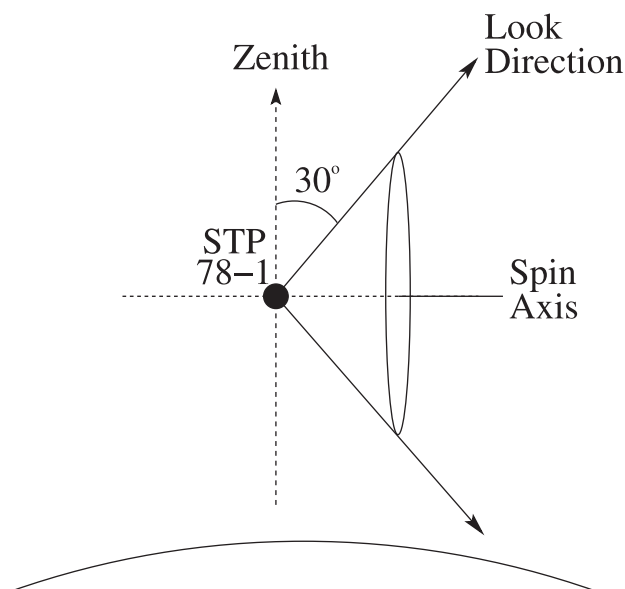
Figure 1. Schematic showing the cone swept out by the field of view of the spectrograph on the STP78-1 satellite. The satellite orbital motion is normal to the plane of the figure. This configuration assures the spectrograph will not look closer than 30° to the Sun.

[9] All data presented here were grouped in 15-s bins, corresponding to a latitude spacing of 1°. The spectra selected were associated with zenith angle in the 145°–150° range. Two look directions were obtained while scanning toward and then away from the nadir during each revolution. For a given zenith angle during one revolution each look direction corresponds to a different region of the atmosphere. Of the two look directions obtained per revolution of the payload, the backward one was selected for analysis.

[10] Figure 2 presents a typical spectrum acquired within the dark auroral oval during active magnetic conditions on 22 March 1979, at 11.15 UT ($Kp = 6^-$). The emissions used to retrieve the energetic electron and proton characteristics have been selected from three criteria. First, we looked among the most intense auroral emissions. Second, we disregarded the emissions that undergo strong multiple

scattering below 600 km, such as O I 130.4 nm, O I 98.9 nm, N I 120.0 nm, and N I 113.4 nm [*Meier et al.*, 1982; *Meier*, 1991]. Third, we selected the emissions for the analysis. H emissions are a unique signature of proton precipitation. We selected H Ly α (121.6 nm) and H Ly β (102.6 nm). The former is used for estimating proton characteristics, the latter (along with the nearby O I 102.7 nm), for validation of the analysis. H Ly α and H Ly β emissions produced within a proton aurora are, for most part, Doppler-shifted and do not undergo resonant scattering. The small component near the rest wavelength is not significantly scattered below 600 km, the altitude of the satellite, due to a low ambient H density (J. Bishop, personal communication, 2000). For electrons we chose non-H emissions whose ratio is a function of the mean energy of the incident particles (see section 4). There are N$_2$ LBH 135.4 nm and O I 135.6 nm, which are not spectrally resolved, and N II 108.5 nm. Even though O I 135.6-nm emission is enhanced by multiple scattering, it is to a much less extent than the other two oxygen lines, O I 130.4 nm and O I 98.9 nm. Multiple scattering affects O I 135.6 nm, but it can be neglected for viewing directions near nadir, which is the case here. The use of the selected emissions for inferring the particle characteristics is explained in section 4.

[11] We selected 22 March 1979, during which a moderate magnetic storm occurred. The magnetic index Kp reached 6^- from 0900 to 1200 UT and 7^- from 1200 to 1800 UT. The solar F$_{10.7}$ index was 183. Preliminary dayglow results associated with this day were presented by *Chakrabarti et al.* [1983]. Figure 3 shows H Ly α brightness over three orbits for that day. Data were integrated between 118.5 and 125.2 nm. The shaded stripes correspond to a solar zenith angle larger than 90°. The black strip near 1445 UT is associated with a time period during which no data were acquired. The H Ly α emission intensities clearly exhibits two components. The smooth, sinusoidal variation corresponds to the geocoronal background produced by resonant scattering of solar photons by the ambient hydrogen atoms of the geocorona. This component depends primarily on the solar zenith angle, with emission maxima for minima in solar zenith angle. The sharp peaks are signatures of proton aurora seen when the spacecraft crosses the auroral oval (magnetic latitudes within 55–75° range). There are strong signatures at night-
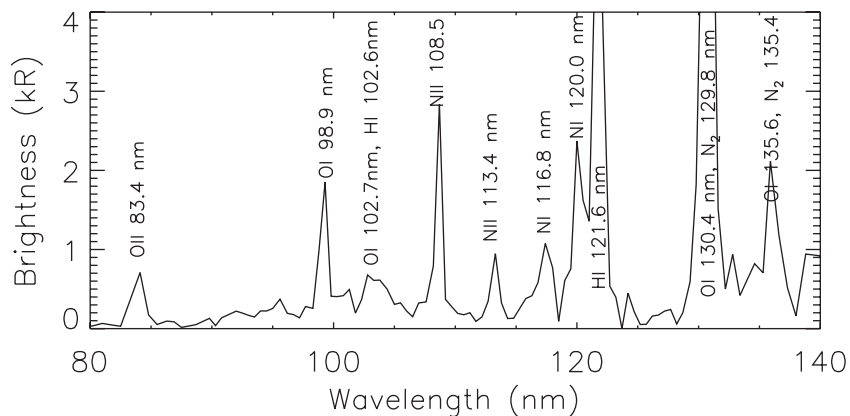
Figure 2. FUV spectrum observed at a magnetic latitude of −63° by STP78-1.
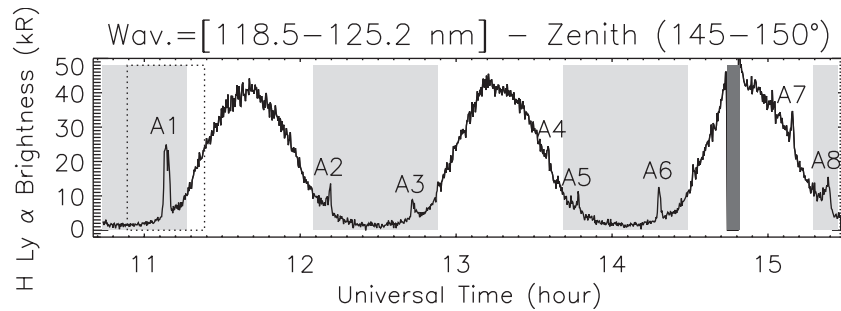
Figure 3. Spectra H Ly α brightness over three orbits of STP78-1 during 22 March 1979 is shown as a function of universal time (UT). The shaded stripes correspond to a solar zenith angle larger than 90°. The black strip at 1445 UT is associated with a time period during which no data were acquired. The smooth, sinusoidal variation is produced by sunlight scattering in the geocorona. The sharp peaks (A1 to A8) correspond to the proton aurora. The A1 region analyzed in this paper is delimited by the dotted box.

side (A1–A3, A5, A6, and A8 in Figure 3), and at dayside (A4 and A7).

[12] For subsequent analysis we focus on the A1 region, delimited by the dotted box. It defines a section of the auroral oval near local midnight over the Southern Hemisphere, around 1100 UT, associated with $Kp = 6^{-}$. The time period of A1 coincides with a large magnetospheric substorm studied by the Coordinated Data Analysis Workshop (CDAW) [*McPherron and Manka*, 1985]. Preliminary characteristics of the H Ly α observations have been described by *Paresce et al.* [1983].

2.2. Removal of the Geocoronal Background

[13] Since geocoronal background is included in the observed auroral H Ly α spectra, we have removed it in order to retrieve the proton aurora component. Note that at nightside the geocoronal component is not seen in the measurements of H Ly β, which thus does not need to be processed.

[14] Figure 4 shows the total signal (solid line) over the A1 region (dotted box in Figure 3) in detector pixels corresponding to successive wavelength bins in the vicinity of H Ly α. The average magnitude of the geocoronal background (dotted line) is estimated from values obtained by fitting the observed brightness outside the "auroral zone" (delimited by the vertical dashed lines) located between −46° and −79° in magnetic latitude. The auroral zone is defined over a large range of latitude to ensure that no proton aurora is present outside this range. The smoothly varying geocoronal background is interpolated across the auroral zone. Note that the enhancement within the auroral zone in the vicinity of 120.0 nm is primarily due to auroral contribution from N I 120.0 nm. In order to solely represent the H Ly α emission, three spectral bins including a large contribution from N I 120.0 nm are disregarded in the subsequent proton aurora fitting process. The total signal and the inferred geocoronal background, integrated over 118.5–125.2 nm, are plotted in Figure 5. Within the strong proton aurora located between −57.5° and −67.0° magnetic latitudes (shaded box in Figure 5), the contribution from the geocoronal background is between 14 and 32% of the observed H I brightness.

[15] Figure 6 presents spectral profiles in the neighborhood of H Ly α for the time period corresponding to the occurrence of the strong proton aurora (shaded box in

Figure 5). The total observed signal is represented with diamonds and the estimated geocoronal background, with crosses. The solid (total signal) and dotted (geocoronal component) lines correspond to a fit to these points with a Gaussian function and a quadratic background term. The proton auroral emission (dashed line) is derived from the two previous curves by subtraction. As expected, the geocoronal profile associated with sunlight scattering is centered at H I 121.6 nm, whereas the auroral profile is Doppler shifted toward the red (by 0.13 nm). This result confirms that the auroral profile is produced by the energetic H atoms within the proton aurora. As most of the emitting H atoms are propagating toward the Earth, that is, away from the spacecraft, the Doppler profile is red shifted from the rest wavelength at 121.6 nm. The total H Ly α brightness consists of 4-kR geocoronal background and 18-kR proton aurora.

3. Model Description

[16] For further analysis of the auroral spectra acquired from STP78-1, we appeal to two kinetic models. The transport of energetic protons in the atmosphere is described by the proton transport code developed by *Galand* [1996], which solves the steady state Boltzmann equations for protons and H atoms coupled through charge-changing reactions. This code has been successfully validated [*Galand et al.*, 1997] by comparison with rocket particle data [*Søraas et al.*, 1974] and by comparison with the model of *Basu et al.* [1993]. The incident flux at the top of the atmosphere is assumed to be purely protons and isotropic over the downward hemisphere. Observations from sounding rockets and from satellites support this pitch angle distribution [e.g., *Søraas et al.*, 1974; *Urban*, 1981]. The incident proton flux is assumed to have a Maxwellian distribution in energy. The mean energy of the Maxwellian (equal to two times the characteristic energy) is varied from 5 to 40 keV, typical for auroral proton precipitation at nightside [*Hardy et al.*, 1989]. The total incident energy flux integrated over pitch angle and energy, Q_0, is chosen as 1 mW m^{-2}, providing normalized results. The incident proton beam is assumed sufficiently broad (larger than 250 km) that beam spreading associated with the horizontal diffusion of the hydrogen atoms can be neglected [*Jasperse and Basu*, 1982]. Collisional angular redistribution is not
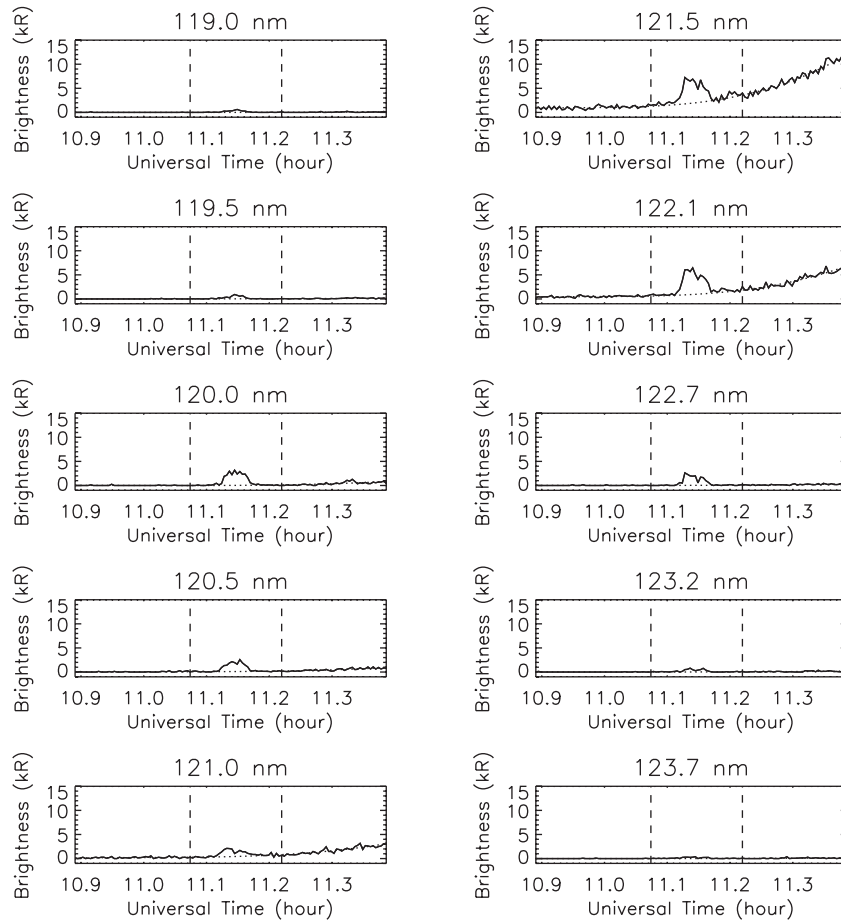
Figure 4. Geocoronal component (dotted line) and total signal (solid line) shown for 10 wavelength bins, each covering a $\sim$0.5 nm band for the A1 region (dotted box in Figure 3). The estimation of the geocoronal background is based on a fit to the signal outside the auroral zone and on an interpolation within the auroral zone defined as the region within the dashed vertical line.

included for simulating the proton transport, because it does not have a significant effect on the integrated excitation rates in the mean energy range considered here [*Galand et al.*, 1998].

[17] The second model we use is the electron transport code developed by *Lummerzheim et al.* [1989]. It describes the transport of the electron population. This population includes incident energetic electrons precipitating into the atmosphere and secondary electrons produced by the interaction of energetic particles (e$^-$, H$^+$, or H) with the atmosphere. It is a multistream code solving the steady state Boltzmann equation for electrons. This model was successfully validated by in situ particle measurements [*Lummerzheim et al.*, 1989] and by laboratory experiment [*Lummerzheim and Lilensten*, 1994]. Precipitating electrons are assumed to have a Maxwellian distribution in energy with a low-energy tail. The mean energy of the Maxwellian is varied from 0.2 to 20 keV. Similar to proton precipitation, the incident electron energy flux is chosen as 1 mW m^{-2}. The source function of the secondary electrons produced inside the proton beam is an output of the proton transport code and an input of the electron transport code. A similar combination of these transport codes was previously performed for the computation of the red line

(O I 630.0 nm) produced inside a proton beam [*Lummerzheim et al.*, 2001].

[18] The neutral atmosphere (N$_2$, O$_2$, and O) adopted in both kinetic models is specified by the Mass Spectrometer and Incoherent Scatter model (MSIS-90) [*Hedin*, 1991], for the location (high-latitude region), magnetic activity ($Kp = 6$), solar activity ($F_{10.7} = 183$), day (22 March 1979), and local time (midnight) of the A1 auroral peak (see Figure 3). No field-aligned electric field or mirroring effect of the magnetic field is considered. The dip angle is 90°. The collision cross section set used for protons is from *Basu et al.* [1987] and from *Rees* [1989] and for electrons, from *Lummerzheim and Lilensten* [1994]. From the computed particle (e$^-$, H$^+$, and H) fluxes, the neutral densities, and the excitation cross sections, it is possible to determine the excitation rate induced by particle impact on neutral species.

[19] The different prompt emissions selected for the analysis (as explained in section 2.1) are as follows: H Ly α, H Ly β, O I 135.6 nm, O I 102.7 nm, N II 108.5 nm, and N$_2$ LBH 135.4 nm. The lifetime of the excited state is very short. No ionospheric model is required to derive the emission rate from the excitation rate. The main source of H emissions is the energetic H atoms produced by charge exchange inside the proton beam. H emission Doppler profiles are computed
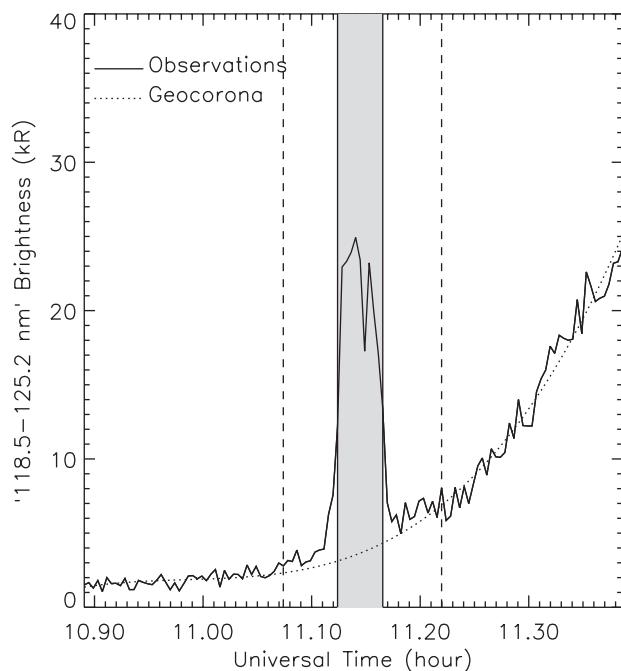
Figure 5. Total (solid line) and inferred geocoronal (dotted) brightnesses, integrated between 118.5 and 125.2 nm, as a function of universal time for the A1 region (dotted box in Figure 3). The dashed vertical lines delimit the auroral zone considered for estimating the geocoronal component (cf. Figure 4). The shaded box defines a region of strong proton aurora spreading over magnetic latitudes from $-67.0°$ to $-57.5°$. Within this region the contribution from the geocoronal background is between 14 and 32% of the observed HI brightness.

by the proton transport code alone. The non-H emissions are usually produced by H^+/H and electron impacts, which requires the use of both transport models.

[20] H Ly α emission cross sections by impact on N_2, O_2, and O by protons (capture) and H atoms (direct excitation) are from *Strickland et al.* [1993]. H Ly β emission cross sections are derived from the previous ones by applying the ratio of oscillator strengths of $H(n = 3)$ to $H(n = 2)$, that is 0.0791/ 0.4162. For O^5S^0 yielding O I 135.6 nm the excitation cross section by H atom impact and electron impact on atomic oxygen is taken from *Edgar et al.* [1975] and *Zipf and Erdman* [1985], respectively. Dissociative excitation of O_2 by electrons is also considered [*Ajello*, 1971], but it is a less significant process compared to the direct excitation of O. The O^5S^0 excitation rate by proton impact is not considered, as it should be insignificant due to the nature of the transition [*Strickland et al.*, 1993]. The excited state O^3D^0 yielding O I 102.7 nm is produced by electron impact on both atomic oxygen [*Vaughan and Doering*, 1988] and molecular oxygen [*Ajello and Franklin*, 1985]. The former is the dominant process. Production of O^3D^0 by H atom impact is not considered in the model due to the lack of cross-section data. N II 108.5-nm emission is produced by electron impact on N_2 through dissociative ionization. The excitation cross sections are from *Aarts and de Heer* [1971]. No H^+ or H impact is included in the model for this emission due to the lack of cross section data. Finally, the emission cross section of N_2 LBH

system originating from the excited state $a^1\Pi_g$ is from *Strickland et al.* [1993] for H^+ and H impact and from *Ajello and Shemansky* [1985] for electron impact. The branching ratio for the vibrational transition leading to N_2 LBH 135.4 nm is 5.2% for electrons [*Vallance-Jones*, 1974]. We apply the same value for protons and H atoms. This is a reasonable assumption provided the vibrational levels of $N_2(a)$ are populated in a similar way by H and H^+ impact as by electron impact (D. Strickland, personal communication, 2000).

[21] The computation of the emission yield (or vertical column-integrated emission rate) requires one to take into account the strong O_2 photoabsorption occurring through dissociative excitation in the Schumann-Runge continuum (130–180 nm). At shorter wavelengths, down to 100 nm, the photoabsorption is still significant but highly variable [*Rees*, 1989]. Photoabsorption cross sections by O_2 are taken from *Hudson* [1971], *Ogawa and Ogawa* [1975], and *Holland et al.* [1993]. The photoabsorption is very strong for H Ly β and O I 102.7 nm ($3.0–3.5\ 10^{-18}$ cm^2) and for N_2 LBH 135.4 nm and O I 135.6 nm ($7.1\ 10^{-18}$ cm^2). The absorption is less intense for N II 108.5 nm ($2.2\ 10^{-19}$ cm^2). The photoabsorption cross section exhibits a deep minimum ($1.0\ 10^{-20}$ cm^2) at the wavelength of H Ly α. The Doppler profile of H Ly α spreads over a wavelength range, which is associated with photoabsorption cross
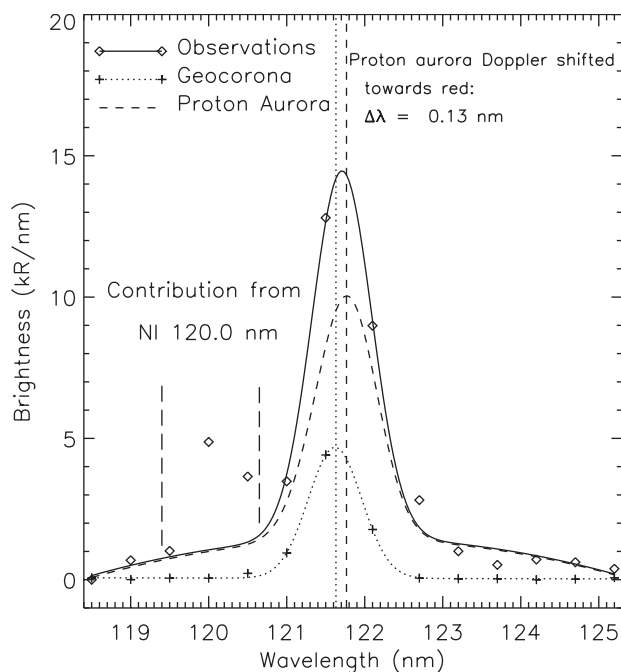
Figure 6. Spectral profiles, in the vicinity of HI 121.6 nm, of the observed signal (solid line) and geocoronal background (dotted line) to the binned data, represented with diamonds and crosses, respectively. The brightnesses have been averaged over the strong proton aurora region (shaded box in Figure 5). Note that the fitting process disregards the three bins in the neighborhood of N I 120.0 nm. The dashed line shows the contribution from the proton aurora derived from the two other profiles. As expected, the geocoronal profile is centered at the rest wavelength H I 121.6 nm (vertical dotted line), whereas the proton aurora profile is Doppler-shifted toward the red (vertical dashed line).
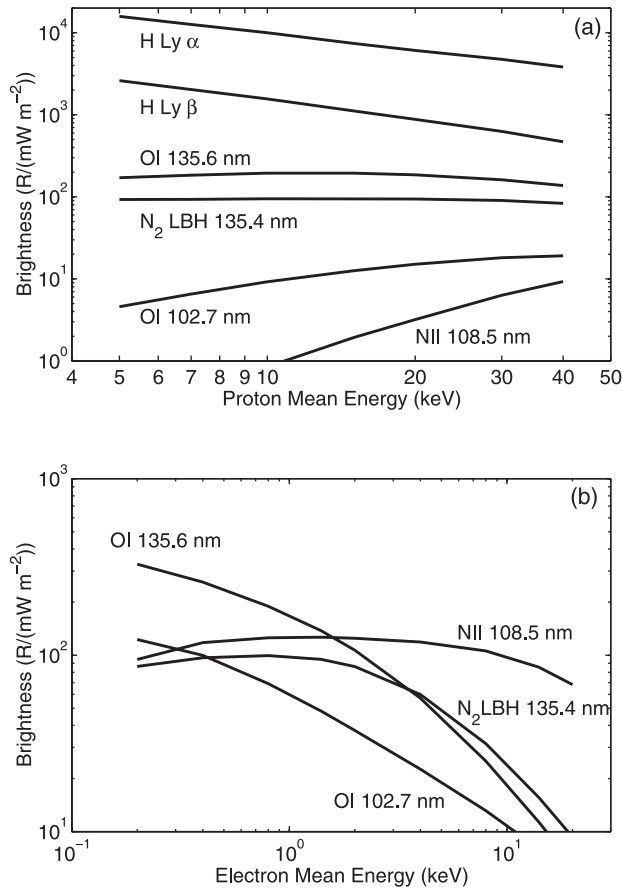
Figure 7. (a) Modeled emission yields as a function of the mean energy of the incident protons. The distribution in energy is assumed to be a Maxwellian with a normalized energy flux of 1 mW m^{-2}. The satellite viewing direction considered is 30° from nadir. (b) The same as the top panel, but for electrons. Note that the distribution in energy for electrons is a Maxwellian with a low-energy tail.

section values between 0.1 and 2.5 10^{-19} cm^2. Overall, it does not suffer significant absorption in the atmosphere.

[22] The modeled yields for the different emissions selected in the analysis are plotted in Figure 7a for protons and in Figure 7b for electrons. The viewing direction chosen is that of the observations, that is, 30° from nadir. With near-nadir viewing direction it is legitimate to assume that the precipitation is uniform in space. Protons in the keV range spend most of their energy in a narrow altitude region [Strickland et al., 1993; Galand and Richmond, 2001], which explains why the emission yields within a proton aurora are not strongly dependent on the mean energy. H emissions, unique to proton precipitation, have an emission yield ratio which is slightly variable, due to the photoabsorption of H Ly β by O$_2$. As the incident proton mean energy increases, the altitude z_0 (where most of the energy is deposited) decreases. The integrated column O$_2$ density at z_0, and thus the photoabsorption, increase with increasing particle mean energy. The dependence of photoabsorption on mean energy is stronger for electron precipitation than for proton precipitation. Unlike protons in the keV energy range, electrons deposit their energy in an altitude region,

which is very wide from the low E region up to the low F region depending on their initial energy [Strickland et al., 1993; Galand and Richmond, 2001]. As a result, the emission yields produced by electrons of higher energies suffer significantly larger absorption than those induced by softer electrons. This result is clearly illustrated in Figure 7b showing emission yields decreasing with increasing electron mean energy. The effect is less for N II 108.5 nm, because the photoabsorption cross section is smaller. For hard electron precipitation, emission yields are very sensitive to the molecular oxygen density.

[23] The electrons produced within a proton aurora are much less energetic than the secondary electrons produced by electron precipitation. For incident protons of low mean energy the produced electrons are too soft to efficiently ionize. Rather, they spend their energy in excitation of the ambient species and, for the softest, in electron heating. Therefore it is not surprising that the emission yield for N II 108.5 nm (whose excited state is produced through ionization) decreases with decreasing mean energy of the incident protons. This decrease is significantly steeper compared with the case of electron precipitation, as illustrated in Figure 7.

[24] The emission yields presented in Figure 7 are in good agreement with those proposed by Strickland et al. [1993]. The only exception concerns the H emissions. The values we obtain for H Ly α yield are a factor of 2 higher than those derived in the other study. The discrepancy is attributed to use of different values for the lower level in the energy grid, 100 eV used here compared to 1 keV for Strickland et al. [1993].

[25] The emission yields presented in Figure 7 cannot be used as such for comparison with observations. The brightnesses of the different emissions (Doppler profile for H emissions) need to be convolved with the instrumental function, in our case a Gaussian function with a FWHM of 0.8 nm. The result of the convolution is binned to the detector spectral bin size of 0.5 nm. The derived spectra for a mean energy of the incident flux of 8 keV for electrons (dashed lines) and 30 keV for protons (dotted lines) are presented in Figure 8. N II 108.5 nm is dominantly produced within the electron aurora (Figure 8a), whereas bins including H emissions are representative of the proton aurora (Figures 8b and 8d). Note that in the presence of pure electron precipitation, the 102–104 nm range is dominated by O I 102.7 nm. Both electron and proton precipitations contribute significantly to N$_2$ 135.4 nm and O I 135.6 nm (Figure 8c). Given the same value for the electron and proton energy fluxes, the percentage of contribution to the N$_2$-O I brightness, here 17% for electrons and 83% for protons, varies with the incident energy of each particle type, as shown in Figure 7.

4. Analysis of the Electron and Proton Auroral Emissions

[26] On the basis of the modeling results shown in section 3, the analysis of the STP78-1 spectra presented in section 2 is performed in three steps. It consists of the derivation of (1) the proton energy flux from H Ly α brightness; (2) the electron mean energy from the brightness ratio of (N$_2$ 135.4 nm, O I 135.6 nm) to N II 108.5 nm; (3) the electron energy
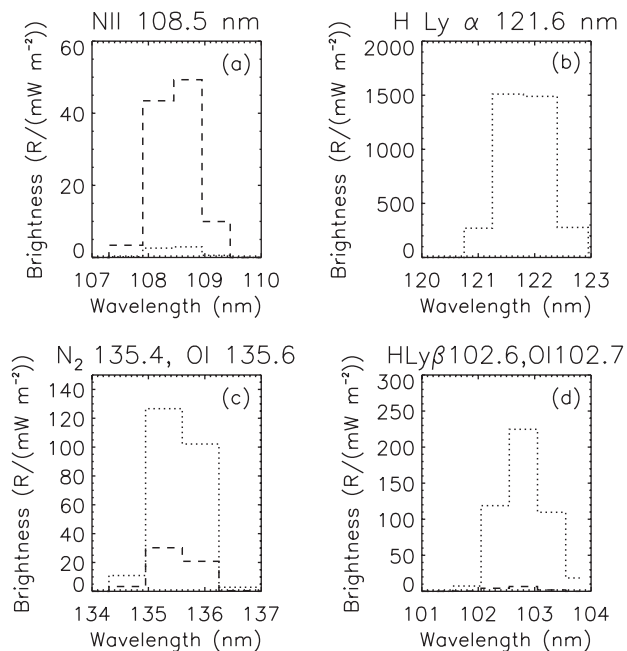
Figure 8. Modeled spectra for different emissions induced by energetic protons (dotted lines) and electrons (dashed lines) binned to the instrument resolution. These spectra have been obtained after convolution of the modeled emission yield (or Doppler profile, for H emissions) with the instrumental function assumed to be triangular with a FWHM of 0.8 nm. The satellite viewing direction considered is 30° from nadir. The distribution in energy of the incident particles is a Maxwellian with, for the electrons, a low energy tail. The mean energies assumed for electrons and for protons are 8 and 30 keV, respectively.

flux from N II 108.5-nm brightness. The validation of the analysis is performed using H Ly β and O I 102.7 nm. Background level, estimated from nearby bins, has been removed from the observed auroral spectra.

4.1. Proton Characteristics

[27] Assuming a distribution in energy and in angle for the incident downward proton flux, it is possible to derive both the mean energy and energy flux of the precipitating protons [*Lummerzheim and Galand*, 2001]. The shape of the Doppler-shifted red wing (blue from ground) is a suitable indicator of the proton mean energy. The total brightness retains information on the energy flux. However, the resolution of the STP78-1 spectrograph is too low to contemplate inferring the proton mean energy from the spectra. Instead, we have fixed the proton mean energy E_m^P to 30 keV, which seems to be a realistic value for nightside proton precipitation during magnetically disturbed conditions ($Kp = 6$). The influence of this choice on the derived particle characteristics is discussed in section 4.3.

[28] The observed brightness in the vicinity of H Ly α, after removal of the geocoronal background (cf. section 2.2), is shown as solid lines in Figures 9a and 9b for two different locations within the A1 region. The modeled spectra for H Ly α (derived as explained in section 3 and for a mean energy of 30 keV) are plotted in dotted lines. The simulated spectra have been matched to the observed

spectra after integration over four bins (121–123 nm). The proton energy flux, which is proportional to the H Ly α brightness, is inferred from this fit and is shown in Figure 9c. The fit is performed only when the observed total brightness is larger than 2 kR, above the noise level. The error bars added in Figure 9c include both the statistical and the calibration uncertainties. The measurement uncertainty yields an error in the proton energy flux of ~20% at the central part of the proton aurora and up to 30% at the edges.

4.2. Electron Characteristics

[29] Figure 10a shows the observed brightness ratio of (N$_2$ 135.4 nm, O I 135.6 nm) to N II 108.5 nm as a function of magnetic latitude, after removing the contribution from proton aurora. The brightness ratio is independent of the particle energy flux, because auroral brightnesses are proportional to this flux. N$_2$ 135.4-nm and O I 135.6-nm emission yields are strongly dependent on the electron mean energy, whereas N II 108.5-nm emission yield is fairly constant (see Figure 7). As a result, the brightness ratio of (N$_2$ 135.4 nm, O I 135.6 nm) to N II 108.5 nm depends on the electron mean energy. A given value of this brightness ratio corresponds to a given value of the electron mean energy, as illustrated in Figure 10b. The stars represent modeled ratios derived from spectra similar to those presented in Figure 8 and integrated over the two spectral bins where the brightness is the
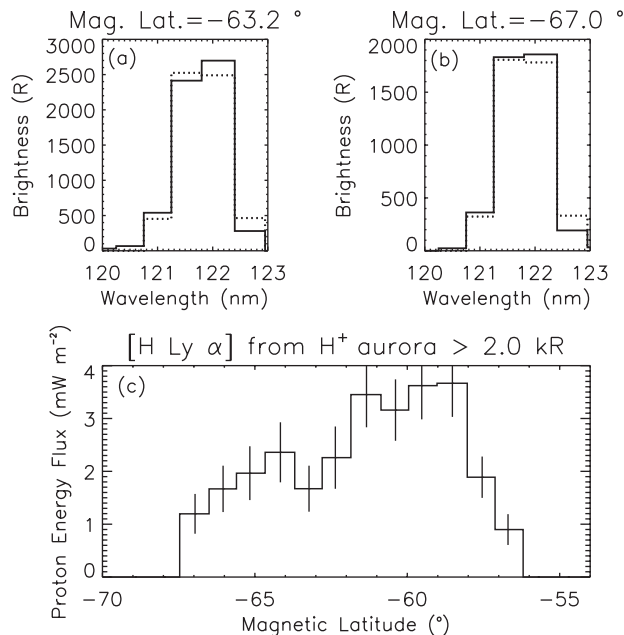
Figure 9. (a and b) Spectra in the vicinity of H Ly α for two different magnetic latitudes, (left) at $-63.2°$ and (right) at $-67.0°$. The observed spectra obtained after removal of the geocoronal background are shown with solid lines. The modeled spectra are shown as dotted lines. (c) Estimated proton energy flux as a function of magnetic latitude. The energy flux is inferred only where the observed H Ly α total brightness - after removal of the geocoronal background - is larger than 2 kR. The error bars are associated with the uncertainties in the measured brightnesses and include both statistical and calibration uncertainties. They represent the standard variation (±1 σ).
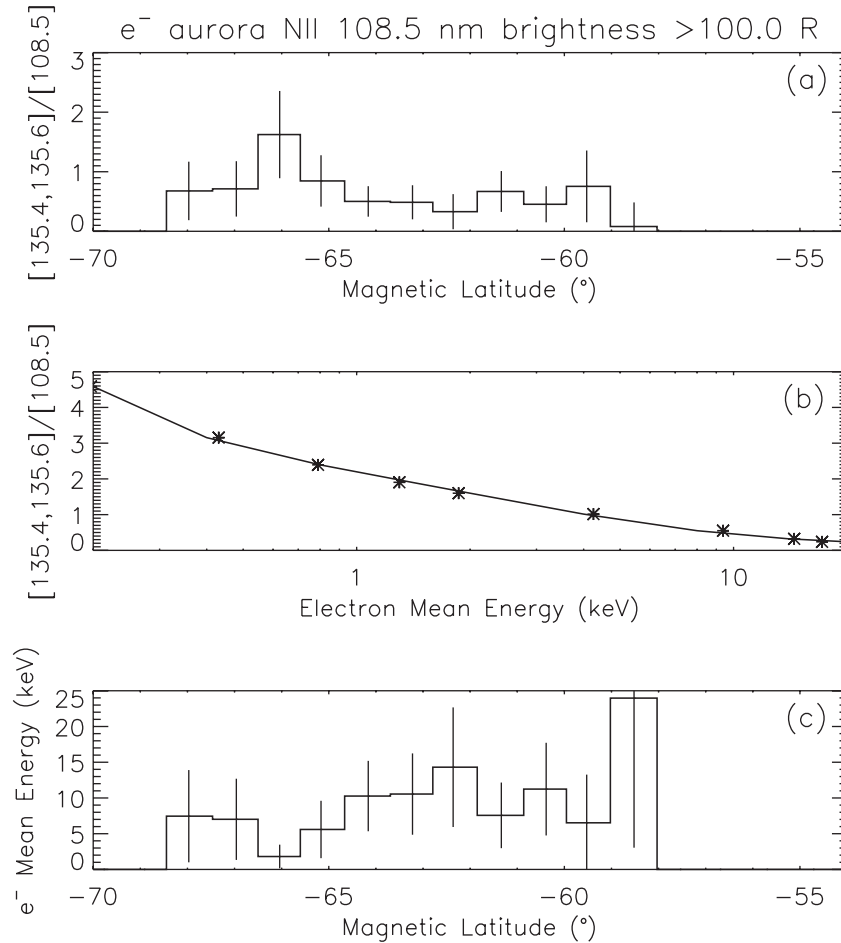
Figure 10.   (a) Observed brightness ratio of (N_2 135.4 nm, O I 135.6 nm) to N II 108.5 nm as a function of magnetic latitude, after removal of the proton contribution. (b) Modeled brightness ratio of (N_2 135.4 nm, O I 135.6 nm) to 108.5 nm as a function of electron mean energy. The distribution in energy of the incident electrons is assumed to be a Maxwellian with a low energy tail. The stars are results of several simulations and the solid line is a fit to these points. (c) Estimated electron mean energy as a function of magnetic latitude. The mean energy is inferred only where the observed N II 108.5 nm total brightness (after removal of the proton contribution) is larger than 100 R. The error bars in (a–c) are associated with the uncertainties in the measured brightnesses and include both statistical and calibration uncertainties. They represent the standard variation (±1 σ).

strongest. The solid line is a fit to these simulated points and is used to retrieve the electron mean energy from the observed ratios. Figure 10c shows the electron mean energy inferred when the N II 108.5-nm brightness of the electron aurora is larger than 100 R. The error bars in Figures 10a and 10c are associated with the measurement uncertainties of the FUV brightnesses. If we except the most equatorward analyzed latitude in Figure 10a, the observed ratio is known within less than 80%. This large uncertainty yields a poor estimation of the electron mean energy, which has error bars between 50 and 100%. The variations seen in the electron mean energy are not real; they can be clearly attributed to the uncertainty in the measurements. The real electron mean energy variation over the auroral oval cannot be resolved due to the large uncertainties in the observations.

[30] Figure 11a shows the observed brightness N II 108.5 nm as a function of magnetic latitude, after removing the proton aurora contributions. The uncertainty in the N II

108.5-nm brightnesses is of the order of 20%. The modeled brightness is plotted as a function of the electron mean energy in Figure 11b. The dependence on mean energy is very weak, which minimizes error propagation from the estimation of the electron mean energy to that of the energy flux. The solid line in Figure 11b is a fit to the simulation results (stars) and is used to estimate the electron energy flux from the N II 108.5-nm brightness shown in Figure 11a. The electron energy flux, derived for N II 108.5-nm brightness larger than 100 R, is plotted in Figure 11c. The error bars associated with the measurements are of the order of 20–30%, except for the most equatorward latitude for which it reaches 70%. This large value can be explained by a high electron mean energy poorly known.

4.3.   Validation of the Analysis

[31] From the estimation of the particle characteristics it is possible to infer the brightness of the different emissions
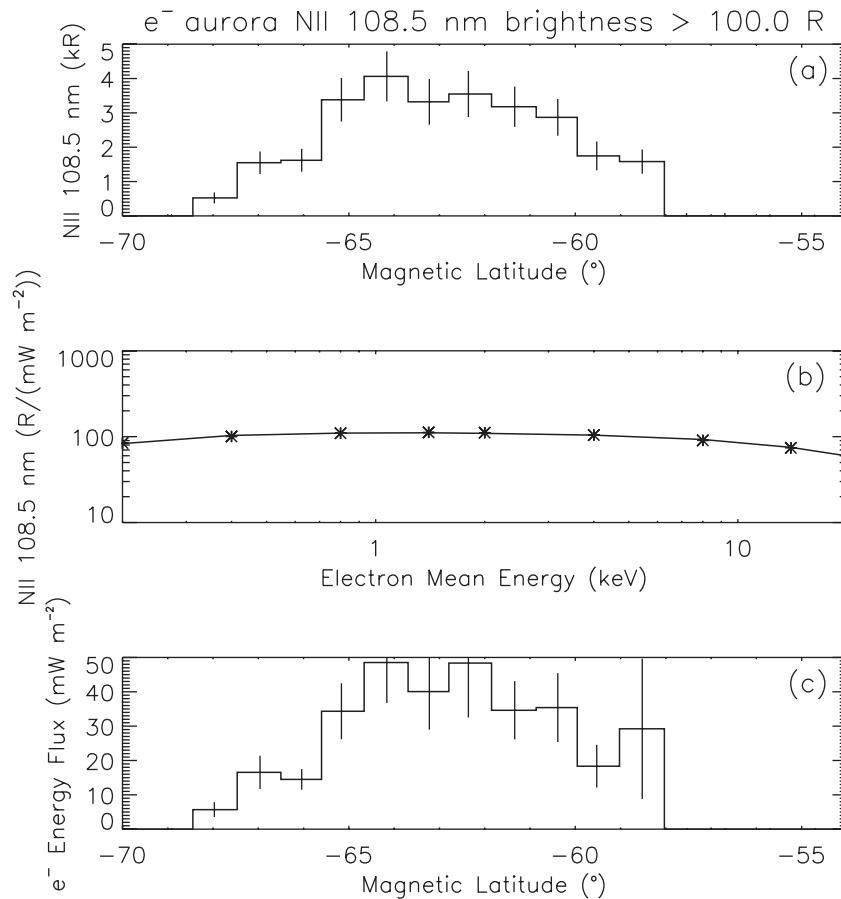
Figure 11. (a) Observed N II 108.5-nm brightness as a function of magnetic latitude, after removal of the proton contribution. (b) Modeled N II 108.5-nm brightness as a function of electron mean energy. The distribution in energy of the incident electrons is assumed to be a Maxwellian with a low-energy tail. The energy flux is normalized to 1 mW m^{-2}. The stars are results of several simulations and the solid line is a fit to these points. (c) Estimated electron energy flux as a function of magnetic latitude. The energy flux is inferred only where the observed N II 108.5-nm total brightness (after removal of the proton contribution) is larger than 100 R. The error bars in (a)–(c) are associated with the uncertainties in the measured brightnesses. This includes both statistical and calibration uncertainties. They represent the standard variation (±1 σ).

selected in this study. Because H Ly α, N II 108.5 nm, N$_2$ 135.4 nm, and O I 135.6 nm were used in the analysis, the agreement between observations (diamonds) and simulated electron (dashed lines) and proton (dotted lines) aurorae is very good, as illustrated in the top three panels in Figure 12.

[32] All the results presented in Figures 9, 10, and 11 are sensitive to the choice of the proton mean energy E_m^P. With a larger value for E_m^P the H Ly α profile extends toward longer wavelengths. After convolution with the instrumental function, this leads to a larger shift of the peak [*Galand et al.*, 1998]. Opposite conclusion is observed for smaller E_m^P. The behavior of the inferred proton energy flux Q_0^P in energy is opposite to that of the H Ly α emission yield illustrated in Figure 7a. The Q_0^P increases with E_m^P. If we consider a value of 40 keV instead of the assumed 30 keV, the emission yield is 25% smaller and the estimated proton energy flux is 25% higher. With a proton energy of 15 keV the proton energy flux is 40% smaller than that obtained for $E_m^P = 30$ *keV*. This error propagates in the estimation of the electron characteristics. The proton contribution to the total 135.4–135.6 nm

brightness varies between ∼15 and 100% from the polar edge to the equator edge of the auroral oval (see Figure 12c). The effect of E_m^P is much less on N II 108.5-nm brightness, because the contribution of proton aurora to this emission is negligible, as seen in Figure 12b. The ratio of (N$_2$ 135.4 nm, O I 135.6 nm) to N II 108.5 nm, and thus the electron mean energy, are affected by the choice of the proton mean energy. For E_m^P increased from 30 to 40 keV, the brightness ratio is 5% smaller (except for the lower ratio value at −58.5° latitude with a peak at 65%). Over the whole latitude range, E_m^e does not increase more than 12%. For E_m^P decreased from 30 to 15 keV, E_m^e is 30% or less smaller. The choice for E_m^P has a less significant effect on the electron mean energy compared to the measurement uncertainties. The variations seen in the electron mean energy distribution in magnetic latitude shown in Figure 10c are mainly due to uncertainties in the observed brightnesses (cf. section 4.2).

[33] The effect of E_m^P on the electron energy flux is expected to be much less than on the electron mean energy,
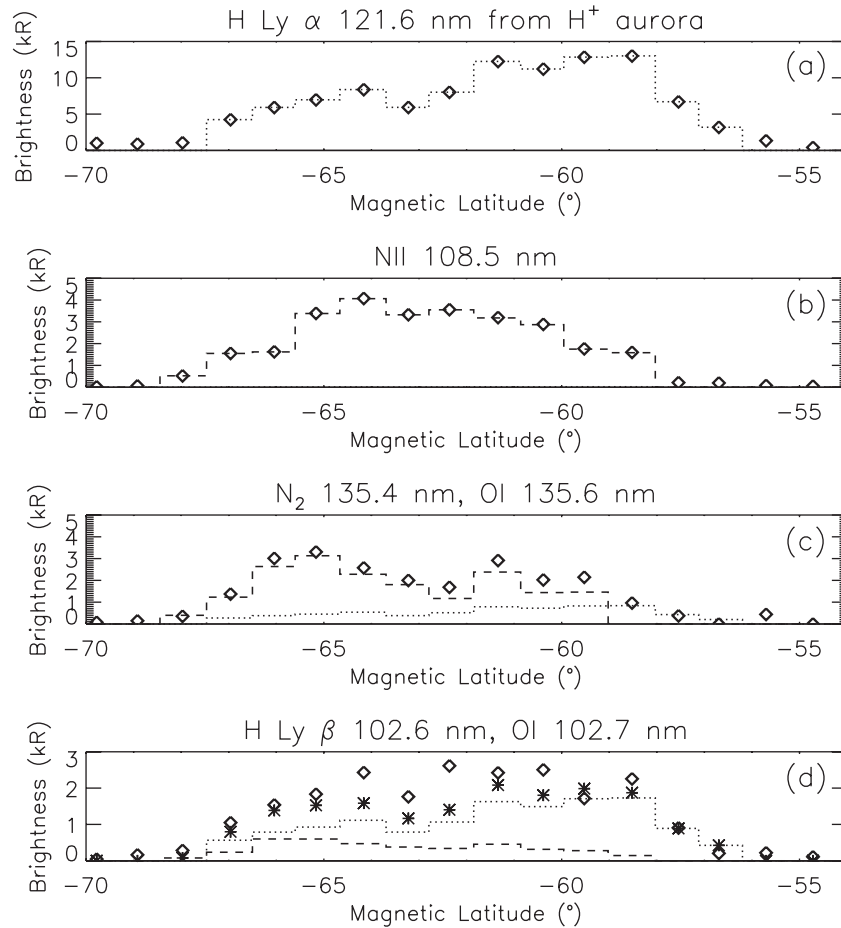
Figure 12. Observed (diamond) and modeled electron-induced (dashed line) and proton-induced (dotted line) brightnesses as a function of magnetic latitude for different auroral emissions: (a) H Ly α produced only in proton aurora; (b) N II 108.5 nm; (c) N_2 135.4 nm and O I 135.6 nm; (d) H Ly β and O I 102.7 nm. The stars represent the modeled brightness from both electron and proton aurora.

because the proton contribution to the N II 108.5-nm brightness is very small and this brightness is relatively independent of the electron mean energy. Except for the equatorward latitude, the variation in E_m^P from 30 up to 40 keV (down to 15 keV) modifies the electron energy flux by less than 1% (4%). At the latitude of $-58.5°$, the variation is larger, with 8% of changes for $E_m^P = 40$ keV and 20% for $E_m^P = 15$ keV compared to an energy of 30 keV.

[34] With no access to simultaneous, colocated particle data, we propose an indirect validation through the brightness of H Ly β and O I 102.7 nm, not used in the analysis. The spectra are integrated over the three bins (102.0–103.5 nm) where the emission is the most intense (see Figure 8d). As illustrated in Figure 12d, there is a reasonable agreement between the observations (diamonds) and the simulated emissions (stars) consisting of the sum of the electron (dashed line) and proton (dotted line) aurorae. Most of the discrepancy can be attributed to the uncertainty in the measurements. The related error bars in 102.0–103.5 nm brightnesses are ~25% in proton-induced aurora and about 100% in electron-induced aurora, reaching values larger than 200% at the edges of the auroral oval. These significant values can be paralleled with the poor estimation of the electron mean energy, mainly a consequence of the signifi-

cant noise in the measurements. Additional sources of uncertainty are the cross sections (20–50% when available), the neutral densities (~30%) used in the model (MSIS-90), and the deviation of the true proton mean energy from the assumed 30-keV value (less than 10%).

4.4. Ionospheric Electrical Conductances

[35] The latitudinal extent of the particle precipitation is illustrated in Figure 13a, which shows the estimated incident electron (dashed line) and proton (dotted line) energy fluxes. The proton aurora is shifted 2° toward the equator from the electron aurora. This result, valid in the midnight sector, agrees with earlier studies based on particle measurements [e.g., *Hardy et al.*, 1989]. As a consequence, protons are the particles which carry most of the energy at the equatorward part of the evening auroral oval. In this region they are the major contributor to Pedersen conductance and, to a lesser extent, to Hall conductance, as shown in Figures 13b and 13c. This conclusion obtained from the analysis of FUV spectra corroborates earlier modeling studies using particle measurements as input [*Galand et al.*, 2001]. For the computation of the conductances we have used the parameterization proposed by *Robinson et al.* [1987] for electrons and by *Galand and Richmond* [2001] for protons.
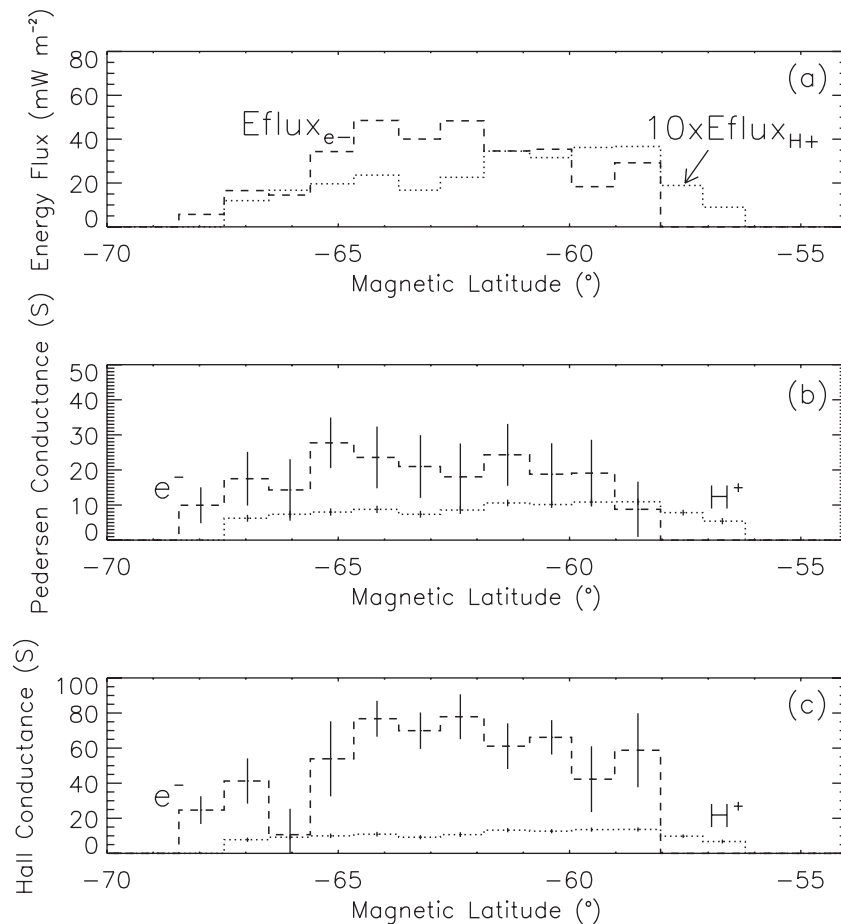
Figure 13. Estimated parameters derived from the analysis of STP78-1 FUV spectra for electron aurora (dashed line) and for proton aurora (dotted line): (a) Particle energy flux (note that the dotted line shows the proton energy flux multiplied by 10); (b) Pedersen conductance; (c) Hall conductance. The error bars are associated with the uncertainties in the measured brightnesses. This includes both statistical and calibration uncertainties. They represent the standard variation (±1 σ).

[36] The shape of the proton-induced conductances (dotted line in Figures 13b and 13c) follows relatively well the energy flux distribution (dotted line in Figure 13a). The proton mean energy is assumed to be constant over magnetic latitude. Note that even for a more realistic mean energy distribution this conclusion would remain valid for the Pedersen conductance, which is fairly independent of the proton mean energy over the 2–40 keV range [*Galand and Richmond*, 2001]. The error bars associated with the measurements are very small for the proton-induced conductances (less than 15% for Pedersen conductance and about 10% for Hall conductance). Unlike protons, electron-induced conductances (dashed line in Figures 13b and 13c) do not follow the energy flux shape as closely. This is a consequence of the strong dependence of electron-induced conductances on mean energy [*Robinson et al.*, 1987]. Large fluctuations in electron-induced conductances, such as that observed at −66° magnetic latitude, are clearly related to the measurement uncertainty. The error in electron-induced conductance calculations is relatively large (on average, 50% for Pedersen conductance and 40% for Hall conductance). This can be explained by the combination of large uncertainties in the electron mean energy (conse-

quence of the noise in the data) and of a strong dependence of the conductances in electron mean energy (in particular at low energies). Note that the total particle-induced conductance can be obtained from $\sqrt{\Sigma_e^2 + \Sigma_P^2}$, where Σ_e and Σ_P are the electron- and proton-induced conductances, respectively [*Galand and Richmond*, 2001]. We find that overall, protons represent 25–30% of the total particle-induced Pedersen conductances.

5. Summary and Discussion

[37] Using a combined electron/proton transport kinetic model, we have been able to derive the incident particle characteristics (energy flux, mean energy) from the analysis of near-nadir FUV spectra observed from space along a poleward path over the southern auroral oval, during magnetically disturbed conditions ($Kp = 6$). The excess H Ly α emission, after removing the geocoronal background, is used to retrieve the incident proton energy flux. Both the mean energy and energy flux of electron precipitation are inferred from non-H emissions (N II 108.5 nm, N$_2$ 135.4 nm, and O I 135.6 nm), after removing the contribution from proton precipitation. Such an approach offers the

opportunity to retrieve both the electron and proton components of the precipitation. This step is crucial, as electrons and protons do not interact in the same way with the atmosphere. Even though the quality of the results is limited by the significant uncertainty in the brightness measurements, the STP78-1 data set has offered us the opportunity to illustrate our approach for inferring particle characteristics from FUV observations. This method may be applicable to upcoming Thermosphere-Ionosphere-Mesosphere Energetics Dynamics (TIMED)/ Global UltraViolet Imager (GUVI) [*Paxton et al.*, 1999] and Defense Meteorological Satellite Program (DMSP)/Special Sensor Ultraviolet Spectrographic Imager (SSUSI) [*Paxton et al.*, 2001] data. In addition to the recent IMAGE satellite, the upcoming TIMED and DMSP missions will provide new insights into the morphology and temporal variability of the energetic precipitating protons.

[38] From the latitudinal distribution of the incident energy flux, the location of the electron and proton aurorae is estimated. Corroborating earlier studies based on direct particle measurements [e.g., *Hardy et al.*, 1989], proton aurora was found to be shifted of a few degrees equatorward from the electron aurora in the evening sector. The estimation of the particle characteristics allows one to infer the Pedersen and Hall electrical conductances induced by particle precipitation. For the studied substorm period, energetic protons contribute significantly to the Pedersen conductance, $\sim25-30\%$ overall of the total particle-induced conductances and much more at the equatorward edge of the midnight aurora. Because protons and electrons do not interact in the same way with the atmosphere, it is crucial to separate electron and proton components of the precipitation while analyzing auroral spectra and estimating the ionospheric state.

[39] The characteristics of the incident particles are derived under the assumption that the energy distribution is a Maxwellian with, for the electrons, a low-energy tail. Such an assumption is usually suitable for electrons [*Strickland et al.*, 1993]. In situ particle measurements have shown that protons have a high-energy tail [e.g., *Basu et al.*, 2001, and references therein]. With this additional flux at high energies, more electrons will be produced and the emission yield will be larger than the one obtained without considering the high-energy tail. Comprehensive studies of high-energy particle measurements (above 20 keV) should be undertaken for a better knowledge of the high energy tail and a more suitable distribution used in models.

[40] The spectral resolution (~0.8 nm) of the STP78-1 FUV spectrometer was not sufficient to infer the proton mean energy E_m^P - we have used a value of 30 keV. Because the H Ly α emission yield is sensitive to E_m^P, such an assumption introduces a large uncertainty on the proton energy flux, as discussed in section 4.3. However, the effect on the electron characteristics is less significant. The derived electron mean energy changes less than 5% in most of the auroral oval when the proton energy is assumed in the $15-40$ keV range. In the present study the uncertainty in the measurements affects the results in a much larger extent. It leads to a poor estimation of the electron mean energy with an error between 50 and 100%. Additional uncertainties are from the cross sections ($20-50\%$ when measured) and from the neutral densities ($\sim30\%$) used in

the modeling. For H^+/H, cross sections are very poorly known for certain reactions, such as the elastic scattering which is significant at low energies (below 1 keV). Excitation or emission cross sections are even sometimes not available, such as that for OI 102.7 nm. Owing to a lack of measurements, N_2 LBH branching ratios are assumed to be equal to the ones for electrons. Laboratory measurements and in situ multi-instrument experiments are drastically needed.

[41] High spectral resolution instruments to observe H emission lines have been deployed from the ground [*Chakrabarti et al.*, 2001; *Robertson et al.*, 2001] and will be extensively used for deriving more information on the incident proton beam than simply the incident energy flux. From space a rocket experiment with both high-resolution spectrometers (≤0.1 nm) and particle detectors will be the most suitable way to estimate as well as improve our ability to infer electron and proton characteristics from FUV observations.

References

Aarts, J. F. M., and F. J. de Heer, Emission cross sections for OI and OII multiplet radiation produced by electron impact on O_2, *Physica*, *56*, 294, 1971.

Ajello, J. M., Dissociative excitation of O_2 in hte vacuum ultraviolet by electron impact, *J. Chem. Phys.*, *55*, 3156, 1971.

Ajello, J. M., and B. Franklin, A study of the extreme ultraviolet spectrum of O_2 by electron impact, *J. Chem. Phys.*, *82*, 2519, 1985.

Ajello, J. M., and D. M. Shemansky, A re-examination of important N_2 cross sections by electron impact with application to the dayglow: The Lyman-Birge-Hopfield band system and NI(119.99 nm), *J. Geophys. Res.*, *90*, 9845, 1985.

Basu, B., J. R. Jasperse, R. M. Robinson, R. R. Vondrak, and D. S. Evans, Linear transport theory of auroral proton precipitation: A comparison with observations, *J. Geophys. Res.*, *92*, 5920, 1987.

Basu, B., J. R. Jasperse, D. J. Strickland, and R. E. Daniell Jr., Transport-theoretic model for the electron-proton-hydrogen atom aurora, *J. Geophys. Res.*, *98*, 21,517, 1993.

Basu, B., D. T. Decker, and J. R. Jasperse, Proton transport model: A review, *J. Geophys. Res.*, *106*, 93, 2001.

Bertaux, J.-L., F. Goutail, and G. Kockarts, Observations of Lyman-α emissions of hydrogen and deuterium, *Science*, *225*, 174, 1984.

Bowyer, S., R. Kimble, F. Paresce, M. Lampton, and G. Penegor, A continuous readout extreme ultraviolet airglow spectrometer, *Appl. Opt.*, *20*, 477, 1981.

Chakrabarti, S., F. Paresce, S. Bowyer, and R. Kimble, The extreme ultraviolet day airglow, *J. Geophys. Res.*, *88*, 4898, 1983.

Chakrabarti, S., D. Pallamraju, J. Baumgardner, and J. Vaillancourt, HiTIES: A High Throughput Imaging Echelle Spectrograph for ground-based visible airglow and auroral studies, *J. Geophys. Res.*, *107*, 30,337, 2001.

Deehr, C., and D. Lummerzheim, Ground-based optical observations of hydrogen emission in the auroral substorm, *J. Geophys. Res.*, *106*, 33, 2001.

Eather, R. H., Auroral proton precipitation and hydrogen emissions, *Rev. Geophys.*, *5*, 207, 1967.

Edgar, B. C., H. S. Porter, and A. E. S. Green, Proton energy deposition in molecular and atomic oxygen and applications to the polar cap, *Planet. Space Sci.*, *23*, 787, 1975.

Frank, L. A., J. B. Sigwarth, J. D. Craven, J. P. Cravens, J. S. Dolan, M. R. Dvorsky, P. K. Hardebeck, J. D. Harvey, and D. W. Muller, The Visible Imaging System (VIS) for the Polar spacecraft, *Space Sci. Res.*, *71*, 297, 1995.

Frey, H. U., S. B. Mende, C. W. Carlson, J.-C. Gerard, B. Hubert, J. Spann,

R. Gladstone, and T. J. Immel, The electron and proton aurora as seen by IMAGE-FUV and Fast, *Geophys. Res. Lett.*, *28*, 1135, 2001.

Galand, M., Transport des protons dans l'ionosphere aurorale, Ph.D. thesis, Univ. Grenoble I, Grenoble, France, 1996.

Galand, M., and A. D. Richmond, Ionospheric electrical conductances produced by auroral proton precipitation, *J. Geophys. Res.*, *106*, 117, 2001.

Galand, M., J. Lilensten, W. Kofman, and R. B. Sidje, Proton transport model in the ionosphere, 1, Multistream approach of the transport equations, *J. Geophys. Res.*, *102*, 22,261, 1997.

Galand, M., J. Lilensten, W. Kofman, and D. Lummerzheim, Proton transport model in the ionosphere, 2, Influence of magnetic mirroring and collisions on the angular redistribution in a proton beam, *Ann. Geophys.*, *16*, 1308, 1998.

Galand, M., R. Roble, and D. Lummerzheim, Ionization by energetic protons in Thermosphere-Ionosphere Electrodynamics - General Circulation Model, *J. Geophys. Res.*, *104*, 27,973, 1999.

Galand, M., T. J. Fuller-Rowell, and M. V. Codrescu, Response of the upper atmosphere to auroral protons, *J. Geophys. Res.*, *106*, 127, 2001.

Germany, G. A., G. K. Parks, M. Brittnacher, J. Cumnock, D. Lummerzheim, J. F. Spann, L. Chen, P. G. Richards, and F. J. Rich, Remote determination of auroral energy characteristics during substorm activity, *Geophys. Res. Lett.*, *24*, 995, 1997.

Hardy, D. A., M. S. Gussenhoven, and D. Brautigam, A statistical model of auroral ion precipitation, *J. Geophys. Res.*, *94*, 370, 1989.

Hedin, A. E., Extension of the MSIS thermosphere model into the middle and lower atmosphere, *J. Geophys. Res.*, *96*, 1159, 1991.

Holland, D. M. P., D. A. Shaw, S. M. McSweeney, M. A. MacDonald, A. Hopkirk, and M. A. Hayes, A study of the absolute photoabsorption, photoionization, and photodissociation cross sections and the photoionization quantum efficiency of oxygen from the ionization threshold to 490 Å, *Chem. Phys.*, *173*, 315, 1993.

Hudson, R. D., Critical review of ultraviolet photoabsorption cross sections for molecules of astrophysical and aeronomic interest, *Rev. Geophys.*, *9*, 305, 1971.

Ishimoto, M., C.-I. Meng, G. J. Romick, and R. E. Huffman, Doppler shift of auroral Lyman α observed from a satellite, *Geophys. Res. Lett.*, *16*, 143, 1989.

Jasperse, J. R., and B. Basu, Transport theoretic solutions for auroral proton and H atom fluxes and related quantities, *J. Geophys. Res.*, *87*, 811, 1982.

Lorentzen, D. A., F. Sigernes, and C. S. Deehr, Modeling and observations of dayside auroral hydrogen emission Doppler profiles, *J. Geophys. Res.*, *103*, 17,479, 1998.

Lu, G., et al., Global energy deposition during the January 1997 magnetic cloud event, *J. Geophys. Res.*, *103*, 11,685, 1998.

Lu, G., M. Brittnacher, G. Parks, and D. Lummerzheim, On the magnetospheric source regions of substorm-related field-aligned currents and auroral precipitation, *J. Geophys. Res.*, *105*, 18,483, 2000.

Lummerzheim, D., and J. Lilensten, Electron transport and energy degradation in the ionosphere: Evaluation of the numerical solution, comparison with laboratory experiments and auroral observations, *Ann. Geophys.*, *12*, 1039, 1994.

Lummerzheim, D., and M. Galand, The profile of the hydrogen H_β emission line in proton aurora, *J. Geophys. Res.*, *106*, 23, 2001.

Lummerzheim, D., M. H. Rees, and H. R. Anderson, Angular dependent transport of auroral electrons in the upper atmosphere, *Planet. Space Sci.*, *37*, 109, 1989.

Lummerzheim, D., M. Brittnacher, D. Evans, G. A. Germany, G. K. Parks, M. H. Rees, and J. F. Spann, High time resolution study of the hemispheric power carried by energetic electrons into the ionosphere during the May 19/20, 1996 auroral activity, *Geophys. Res. Lett.*, *24*, 987, 1997.

Lummerzheim, D., M. Galand, J. Semeter, M. J. Mendillo, M. H. Rees, and F. J. Rich, Emission of OI(630 nm) in proton aurora, *J. Geophys. Res.*, *106*, 141, 2001.

Meier, R. R., Ultraviolet spectroscopy and remote sensing of the upper atmosphere, *Space Sci. Rev.*, *58*, 1, 1991.

Meier, R. R., R. R. Conway, P. D. Feldman, D. J. Strickland, and E. P. Gentieu, Analysis of nitrogen and oxygen far ultraviolet auroral emissions, *J. Geophys. Res.*, *87*, 2444, 1982.

Meinel, A. B., Doppler-shifted auroral hydrogen emission, *Astrophys. J.*, *113*, 50, 1951.

Mende, S. B., H. U. Frey, M. Lampton, J.-C. Gerard, B. Hubert, S. Fuselier, J. Spann, R. Gladstone, and J. L. Burch, Global observations of proton and electron auroras in a substorm, *Geophys. Res. Lett.*, *28*, 1139, 2001.

Miller, J. R., and G. G. Shepherd, Rocket measurements of H_β production in a hydrogen aurora, *J. Geophys. Res.*, *74*, 4987, 1969.

Ogawa, S., and M. Ogawa, Absorption cross sections of $O_2(a^1\Delta_g)$ and $O_2(X^3\Sigma_g)$ in the region from 1087 to 1700 Å, *Can. J. Phys.*, *53*, 1845, 1975.

Paresce, F., S. Chakrabarti, S. Bowyer, and R. Kimble, The extreme ultraviolet spectrum of dayside and nightside aurorae: 800-1400, *J. Geophys. Res.*, *88*, 4905, 1983.

Paxton, L. J., et al., Global ultraviolet imager (GUVI): Measuring composition and energy inputs for the NASA Thermosphere Ionosphere Mesosphere Energetics and Dynamics (TIMED) mission, *SPIE Opt. Spectroscopic Techn. Instrum. Atmos. Space Res. III*, *3756*, 265, 1999.

Paxton, L. J., D. Morrison, H. Kil, Y. Zhang, B. S. Ogorzalek, and C. Meng, Validation of remote sensing products produced by the Special Sensor Ultraviolet Scanning Imager (SSUSI): A far UV imaging spectrograph on DMSP F-16, *SPIE Opt. Spectroscopic Techn. Instrum. Atmos. Space Res. IV*, *4485*, in press, 2001.

Reasoner, D. L., R. H. Eather, and B. J. O'Brien, Detection of alpha particles in auroral phenomena, *J. Geophys. Res.*, *73*, 4185, 1968.

Rees, M. H., *Physics and Chemistry of the Upper Atmosphere, Cambridge Atmos. Space Sci. Ser.*, Cambridge Univ. Press, New York, 1989.

Robertson, S. C., I. Furniss, I. McWhirter, S. Lanchester, A. D. Aylward, M. H. Rees, T. S. Trondesen, and A. P. Van Eyken, Proton and electron auroras over Svalbard following an IMF shock, European Geophysical Society (EGS), XXVI General Assembly, Nice, France, GRA3, 6655, ST13, March 25–30, 2001.

Robinson, R. M., R. R. Vondrak, K. Miller, T. Dabbs, and D. Hardy, On calculating ionospheric conductances from the flux and energy of precipitating electrons, *J. Geophys. Res.*, *92*, 2565, 1987.

Romick, G. J., and R. D. Sharp, Simultaneous measurements of an incident hydrogen flux and the resulting hydrogen Balmer α emission in an auroral hydrogen arc, *J. Geophys. Res.*, *72*, 4791, 1967.

Søraas, F., H. R. Lindalen, K. Mâseide, A. Egeland, T. A. Sten, and D. S. Evans, Proton precipitation and the H_β emission in a postbreakup auroral glow, *J. Geophys. Res.*, *79*, 1851, 1974.

Strickland, D. J., R. E. Daniell Jr., J. R. Jasperse, and B. Basu, Transport-theoretic model for the electron-proton-hydrogen atom aurora. 2. Model results, *J. Geophys. Res.*, *98*, 21,533, 1993.

Strickland, D. J., J. Bishop, J. S. Evans, T. Majeed, R. J. Cox, D. Morrison, G. J. Romick, J. F. Carbary, L. J. Paxton, and C.-I. Meng, Midcourse Space Experiment/Ultraviolet and Visible Imaging and Spectrographic Imaging limb observations of combined proton/hydrogen/electron aurora, *J. Geophys. Res.*, *106*, 65, 2001.

Takahashi, Y., and H. Fukunishi, The dynamics of the proton aurora in auroral breakup events, *J. Geophys. Res.*, *106*, 45, 2001.

Urban, A., Measurements of low energy auroral ions, *Planet. Space Sci.*, *29*, 1353, 1981.

Vallance-Jones, A., *Aurora D. Reidel*, Norwell, Mass., 1974.

Vallance-Jones, A., F. Creutzberg, R. L. Gattinger, and F. R. Harris, Auroral studies with a chain of meridian-scanning photometers, 1, Observations of proton and electron aurora in magnetospheric substorms, *J. Geophys. Res.*, *87*, 4489, 1982.

Vaughan, S. O., and J. P. Doering, Absolute experimental differential and integral electron excitation cross sections for atomic oxygen 4. The $(^3P \rightarrow 3s'' \, ^3P^0)$, $(^3P \rightarrow 2s \, 2p^{53} P^0)$, $(^3P \rightarrow 4d' \, ^3P^0)$ autoionizing transitions (878, 792, and 770 Å) and five members of the $(^3P \rightarrow nd \, ^3D^0)$ Rydberg series (1027 Å), *J. Geophys. Res.*, *93*, 289, 1988.

Vegard, L., Emission spectra of night sky and aurora, Reports of the Gassiot Committee, *Phys. Soc. London*, *82*, 1948.

Whalen, B. A., I. B. McDiarmid, and E. E. Budzinski, Rocket measurements in proton aurora, *Can. J. Phys.*, *45*, 3247, 1967.

Wiens, R. H., and A. Vallance-Jones, Studies of auroral hydrogen emissions in West Central Canada, III. Proton and electron auroral ovals, *Can. J. Phys.*, *47*, 1493, 1969.

Zipf, E. C., and P. W. Erdman, Electron impact excitation of atomic oxygen: Revised cross sections, *J. Geophys. Res.*, *93*, 11,087, 1985.

─────────────

B. C. Bush, Atmospheric Research Laboratory, Scripps Institute of Oceanography, University of California, San Diego, CA 92037, USA.

S. Chakrabarti and M. Galand, Center for Space Physics, Boston University, Boston, MA 02215, USA. (mgaland@bu.edu)

D. Lummerzheim, Geophysical Institute, University of Alaska, Fairbanks, AK 99775, USA.

A. W. Stephan, Computational Physics, Inc., Springfield, VA 22151, USA.